Adv. Radio Sci., 15, 269–281, 2017
https://doi.org/10.5194/ars-15-269-2017

Advances in Radio Science
Open Access Proceedings

Design of a carrier-depletion Mach-Zehnder modulator in 250 nm silicon-on-insulator technology

María Félix Rosa, Lotte Rathgeber, Raik Elster, Niklas Hoppe, Thomas Föhn, Martin Schmidt, Wolfgang Vogel, and Manfred Berroth

University of Stuttgart, Institute for Electrical and Optical Communications Engineering, Stuttgart, Germany

Correspondence to: María Félix Rosa (maria.felix-rosa@int.uni-stuttgart.de)

Received: 15 January 2017 – Revised: 18 September 2017 – Accepted: 19 October 2017 – Published: 5 December 2017

Abstract. We present the design of a single-drive Mach-Zehnder modulator for amplitude modulation in silicon-on-insulator technology with 250 nm active layer thickness. The applied RF signal modulates the carrier density in a reverse biased lateral pn-junction. The free carrier plasma dispersion effect in silicon leads to a change in the refractive index. The modulation efficiency and the optical loss due to free carriers are analyzed for different doping configurations. The intrinsic electrical parameters of the pn-junction of the phase shifter like resistance and capacitance and the corresponding RC-limit are studied. A first prototype in this technology fabricated at the IMS CHIPS Stuttgart is successfully measured. The structure has a modulation efficiency of $V_\pi L = 3.1\,\mathrm{V{\cdot}cm}$ at 2 V reverse bias. The on-chip insertion loss is 4.2 dB. The structure exhibits an extinction ratio of around 32 dB. The length of the phase shifter is 0.5 mm. The cutoff frequency of the entire modulator is 30 GHz at 2 V. Finally, an optimization of the doping structure is presented to reduce the optical loss and to improve the modulation efficiency. The optimized silicon optical modulator shows a theoretical modulation efficiency of $V_\pi L = 1.8\,\mathrm{V{\cdot}cm}$ at 6 V bias and a maximum optical loss due to the free carrier absorption of around $3.1\,\mathrm{dB\,cm^{-1}}$. An ultra-low fiber-to-fiber loss of approximately 4.8 dB is expected using the state of the art optical components in the used technology.

1 Introduction

Backhaul nets rely on custom made high-speed electro-optical components. The ever increasing data rates and associated rising complexity and costs are the main driver for the integration of complete optical systems on a single die. One of the key components of such a system is the optical modulator. High modulation efficiency, small size, low driving voltage, high extinction ratio (ER), low optical loss and wide bandwidth are the figures of merit of the modulators to be optimized.

During the last years our group has presented CMOS compatible grating couplers (GC) with a record coupling efficiency of $\eta = -0.62\,\mathrm{dB}$ (Zaoui et al., 2014) in a 250 nm silicon-on-insulator (SOI) platform fabricated at the Institut für Mikroelektronik Stuttgart (IMS CHIPS). The low losses of the fiber-to-chip coupling (Zaoui et al., 2014) or polarization splitting (Zaoui et al., 2013) are an important benefit to reduce the total loss of the optical modulator. Due to this fact a first design of a silicon optical modulator utilizing this technology is realized in this work serving as a preparative step for the fabrication of a low loss and highly efficient modulator in a CMOS compatible technology.

The influence of the doping concentration and the geometry of the phase shifter on the modulator performance for different technologies are investigated in the literature (e.g., Petousi et al., 2013; Goykhman et al., 2013). Based on these works we present the study of the influence of the most important design parameters of the modulator in the novel technology developed by IMS CHIPS using 250 nm active Si instead of the standard 220 nm. First, the geometry of the waveguide is calculated for a single mode propagation and low loss. Then, an analysis of the doping influence on the modulation efficiency performance and optical loss is done for the fabrication of a prototype. The measurement results of the fabricated device are presented in this work as a validation. Furthermore, an optimization of the doping is realized to improve the modulation efficiency and optical loss of the

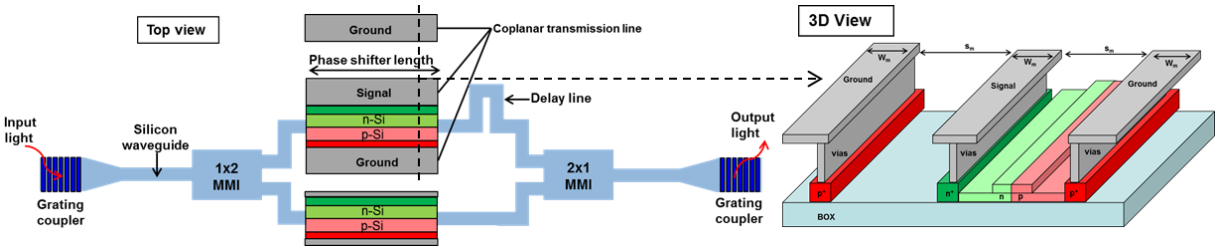

Figure 1. Scheme of the designed Mach-Zehnder modulator.

structure. Finally, the results are compared with the work of other research groups.

2 Design of the device

In this work a silicon optical modulator is simulated for fabrication in the IMS CHIPS technology for the first time. The used SOI-wafer has a 625 µm thick silicon substrate with a 3 µm thick buried oxide (BOX) layer. On top is a 250 nm thick active silicon layer in which the components are structured. The SOI-wafer is passivated with a 1 µm thick SiO_2 layer. A 500 nm thick aluminum metal layer is added and structured on top of the processed wafer. The active silicon is connected to the top metal through vias.

The design consists of a single-drive Mach-Zehnder modulator (MZM) for amplitude modulation (Fig. 1). Two transversal electric (TE) mode grating couplers followed by a linear taper couple the light between single mode fibers and the 400 nm wide waveguides. A 1×2 multimode interference coupler (MMI) splits the light uniformly in both interferometer arms. Two branches of doped waveguides, one of them connected to an RF coplanar line through vias, perform the modulation. Another 2×1 MMI acts as power combiner. Both waveguides are doped to get similar optical loss in both branches and hence to maximize the ER of the modulator. Only one arm is driven during modulation for an easier characterization and comparison with the simulations. A delay line is added in one branch to increase the optical path difference (OPD) resulting in a reduction of the free spectral range in the optical transmission spectrum. Hence, the phase shift produced by the modulator section can be easily observed by analyzing a small wavelength range. The modulation relies on the free carrier plasma dispersion effect: a pn-junction allows to modulate the free carrier density locally in the waveguide core with an external DC or RF voltage. A change in the density of free carriers leads to a change in the refractive index Δn, but also to a change in the attenuation $\Delta\alpha$ (Soref and Bennett, 1987).

3 Estimation of the ridge waveguide geometry

The research on the geometric dimensions is carried out by simulating the mode profiles in a ridge waveguide for a wavelength of 1550 nm. In Fig. 2a the most important geometric parameters are described. The height $h = 250$ nm is determined by the thickness of the silicon layer of the wafer. For the optimization of the waveguide width, it is considered that only the fundamental TE mode should be guided in the core in order to avoid multimode interference. For narrow waveguides the mode is not well confined in the silicon waveguide core. Therefore, the attenuation α is high if additional absorption due to highly doped Si or metal regions occurs. Hence, the waveguide core should be designed as wide as possible. However, for a core width of 420 nm and above, the second order TE mode can propagate as well. Thus, the waveguide width is set to $w = 400$ nm.

The RF metal lines are connected through metal vias to a 250 nm thick highly doped Si region for a better ohmic contact. The height of the silicon underneath the metal contact should not be too small, particularly if the height h_{sl} is very small. Then, the contact resistance between metal and the doped silicon is much lower and the influence of process variations is minimized.

The distance s between the metal vias and the silicon waveguide core has a huge influence on the attenuation of the optical signal, since the highly doped Si ($\sim 10^{20}\,\mathrm{cm}^{-3}$) and the metal, with a complex refractive index $n = n + i\kappa$, strongly attenuate the optical modes. This means, on the one hand, that the distance s should be chosen to be as large as possible. On the other hand, it has to be taken into account that for a greater distance s, the electrical resistance also increases weakening the electrical performance of the device. In Fig. 2b the calculated total resistance R in Ωcm (to calculate the resistance in Ω, the resistance R has to be divided by the phase shifter length L) of the slabs is plotted for different slab thickness h_{sl} depending on the distance s. R_n and R_p are the resistances in Ωcm of the n- and p-doped slabs.

$$R = R_n + R_p = \frac{s \cdot \rho_n}{h_{sl}} + \frac{s \cdot \rho_p}{h_{sl}} \tag{1}$$

The resistance (if the slabs are lowly doped) is analytically calculated for two different doping densities, being N_a and N_d the doping concentration of the p- and n-doped regions.

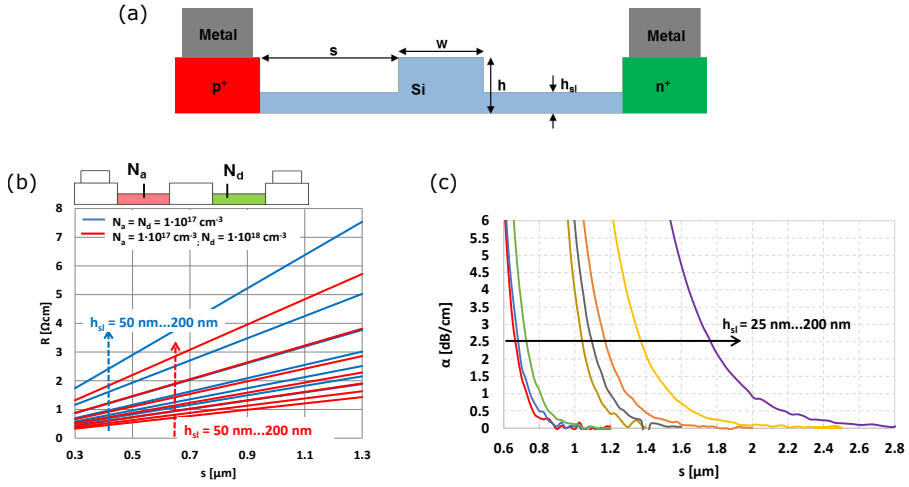

Figure 2. (a) Scheme of the silicon ridge waveguide with the contact regions. **(b)** Calculated total resistance (in Ωcm) of the slabs depending on the thickness h_{sl} and the length of the slabs s for two different doping concentrations. N_{a} (acceptors) and N_{d}(donors). **(c)** Simulation of the loss depending on the distance s for different slab thicknesses h_{sl} ($h = 250\,\mathrm{nm}$, $w = 400\,\mathrm{nm}$).

The parameters ρ_{n} and ρ_{p} are the resistivity of the n- and p-doped silicon.

In addition, the attenuation is significantly greater at the same distance s, if a higher proportion of the electric field of the propagation light is present in the region of the metal contact. Therefore, the ratio h_{sl}/h should be as small as possible to keep the optical mode confined in the waveguide core. Figure 2c shows the attenuation over the distance s (of the structure with intrinsic Si core and slabs as shown in Fig. 2a) for different slab thicknesses h_{sl}. As the heighth_{sl} increases, the distance in which the metal should be positioned to obtain the same attenuation shifts to larger values.

The slab thickness $h_{\mathrm{sl}} = 50\,\mathrm{nm}$ is chosen to keep the optical mode confined in the core of the waveguide. That maximizes the modulation due to the carrier-depletion in the core of the waveguide. Hence, the minimum spacing of the metal chosen in the following is $s = 1.25\,\mu\mathrm{m}$ to minimize the optical loss.

4 Doping profile

The next step in the design of the modulator is to optimize the doping profile. The result of the calculated parameters Δn_{eff} and α depends on the doping of the waveguide. The simulations are realized with the commercial software RSoft from Synopsys®. The finite element method (FEM) is used to simulate the propagating and leaky modes of the doped waveguide cross section. The carrier effect is included in the simulations by utilizing the Multi-Physics Utility of the software. The change of the optical refractive index and the absorption generated by the free carrier distributions is determined from the model described in Soref and Bennett (1987).

The influence of the doping concentration requires a balancing between these parameters: a higher doping concentration allows for a higher change of the effective refractive index Δn_{eff}, but the optical loss increases with the free carrier density. The distance from the p^+- and n^+-type doped regions to the waveguide core is s_{p} and s_{n}, respectively. For a good ohmic contact, the high doping concentration is determined as $N_{\mathrm{a+,d+}} = 1 \times 10^{20}\,\mathrm{cm}^{-3}$.

Three different doping profiles of the waveguide core are depicted in Fig. 3. The doping concentration for the lowly doped regions is $N_{\mathrm{a,d}} = 1 \times 10^{17}\,\mathrm{cm}^{-3}$. In this section the distances s_{n} and s_{p} are the same as $s = 1.25\,\mu\mathrm{m}$ to analyze the loss caused only for the carrier absorption of the low doping. In Sect. 7 these distances are varied to optimize the structure. The attenuation α is always given at 0 V since for higher bias voltages the free carrier density in the waveguide core is lower. The simulation results of the different doping profiles are presented in Fig. 4.

A purely p-doped core is compared to a purely n-doped core. For p-type doping a Δn_{eff} more than three times higher than for n-type doping is obtained at the same voltage (Fig. 4a). Besides, the attenuation is lower for p-type doping (Fig. 4b). The results for the pn-doped core (p/n doped-curve) are analyzed in detail. In this case the change of the effective refractive index Δn_{eff} rises with the reverse voltage faster than for the purely p-doped core, but it flattens for higher reverse voltages (Fig. 4a). The attenuation is lower than for the purely p- or n-doped core from 0 to 6 V and also decreases with the reverse voltage until the curve flattens (Fig. 4b). The effect of charge carrier-depletion is therefore significantly greater than for purely p-type doping. Figure 4c shows a comparison of the modulation efficiency ($V_\pi L$) and the figures of merit that combine the modulation efficiency with the respective optical loss due to the free carrier absorp-

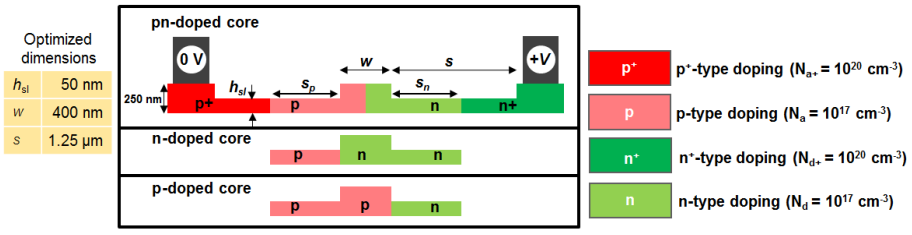

Figure 3. Scheme of the different parameters regarding the geometry and doping of the modulator. Three variants of the doping profile are simulated (pn-, n- and p-doped core). The values of the parameters h, h_{sl}, w and s are fixed.

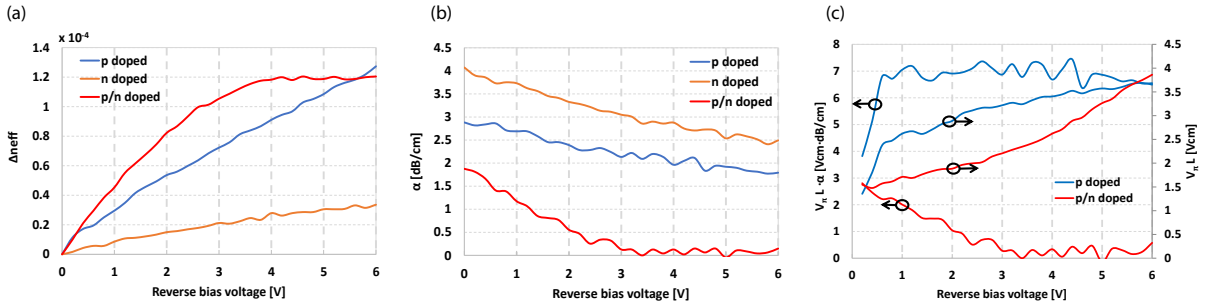

Figure 4. Simulations of **(a)** the change of the effective refractive index, **(b)** the attenuation, **(c)** modulation efficiency and $V_\pi L \cdot \alpha$ depending on the reverse bias voltage for different doping profiles in the waveguide core ($s_p = s_n = s = 1.25\,\mu\text{m}$; $h_{sl} = 50\,\text{nm}$; $N_a = N_d = 1 \times 10^{17}\,\text{cm}^{-3}$).

tion ($V_\pi L \cdot \alpha$) of the two doping profiles (pn- and p-doped cores). The modulation efficiency is calculated as

$$V_\pi L = \frac{\lambda \cdot V}{2 \cdot \Delta n_{\text{eff}}} = \frac{\lambda \cdot V}{2(n_{\text{eff}}(V) - n_{\text{eff}}(V = 0V))}, \quad (2)$$

being $\lambda = 1550\,\text{nm}$ the wavelength, V the reverse bias voltage, $n_{\text{eff}}(V)$ the effective index at the applied bias voltage V and $n_{\text{eff}}(V = 0\,V)$ the effective index at the voltage $V = 0\,\text{V}$.

The pn-doped core exhibits a better performance in the modulation efficiency till 5.5 V with respect to the p-doped core design. For higher bias voltages the p-doped core design has a better modulation efficiency (i.e., lower $V_\pi L$). The $V_\pi L \cdot \alpha$ is noticeably lower for the pn-doped due to the reduction in the loss caused by the decrease of free carriers in the core of the waveguide because of the depletion (see Fig. 5). The simulations show a $V_\pi L = 1.9\,\text{V·cm}$ and approximately $V_\pi L \cdot \alpha = 1\,\text{V·dB}$ at 2 V for the pn-doped core and $V_\pi L = 2.9\,\text{V·cm}$ and around $V_\pi L \cdot \alpha = 7\,\text{V·dB}$ at 2 V for the p-doped core. At the bias voltage of 6 V compared to 2 V the simulation results show for the pn-doped core design a stronger change in figure of merit: $V_\pi L = 3.9\,\text{V·cm}$ and $V_\pi L \cdot \alpha = 0.6\,\text{V·dB}$. The p-doped core changes significantly less in the values obtained: $V_\pi L = 3.7\,\text{V·cm}$ and $V_\pi L \cdot \alpha = 6.5\,\text{V·dB}$.

Figure 5 is shown as example of the working principle of the simulated p- and pn-doped waveguide core for a better understanding of the simulation results of Fig. 4. A comparison of the free carrier distribution of both structures is depicted for different reverse bias voltages. In the p-doped case, which is shown in the left column of the figure, the free charge carriers are present in the core and migrate with the voltage. The depletion region is formed at the edge of the core. However, the maximum of the optical electric field lies in the center of the waveguide and only a small portion overlaps with the region of the charge carrier-depletion. The situation is different in the pn-doped waveguide, shown on the right column of Fig. 5. Here, there is a depleted region at 0 V in the center of the waveguide, where the maximum of the electric field is placed. Thus, the attenuation is smaller than in the p-doped case. When the voltage is applied, electrons and holes move and the depletion region expands. For a reverse bias voltage between 0 and 3 V (Fig. 5b, c) the high change in the free carrier concentration occurs in the waveguide core. Here, the optical field is confined, therefore the Δn_{eff} is large and also the modulation efficiency. When the applied reverse voltage exceeds 4 V the depletion region is wider than the waveguide core (Fig. 5d) and the Δn_{eff} starts to flatten (Fig. 4a), since almost all free carriers are removed.

The modulation performance could be improved by further optimization of the doping concentration. That is realized for the case of the p-doped waveguide core in Sect. 7. The fabrication of the pn-doped core is a technological challenge because misalignments could produce a wide undoped region. That results in a significant deterioration of the modulation efficiency of the device. Therefore, for our first prototype the p-doped core type is chosen.

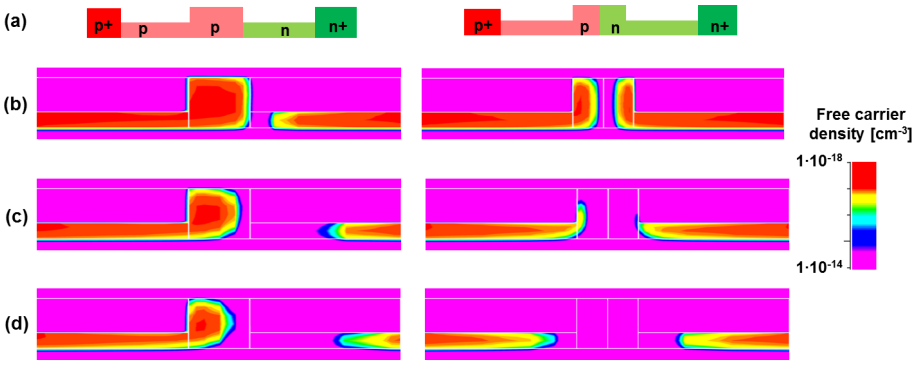

Figure 5. (a) Doping profile of a p-doped (left) and pn-doped (right) waveguide ($N_a = N_d = 1 \times 10^{17}$ cm^{-3}). **(b)** Free carrier concentration for the applied reverse bias voltage of 0 V, **(c)** 3 V and **(d)** 6 V.

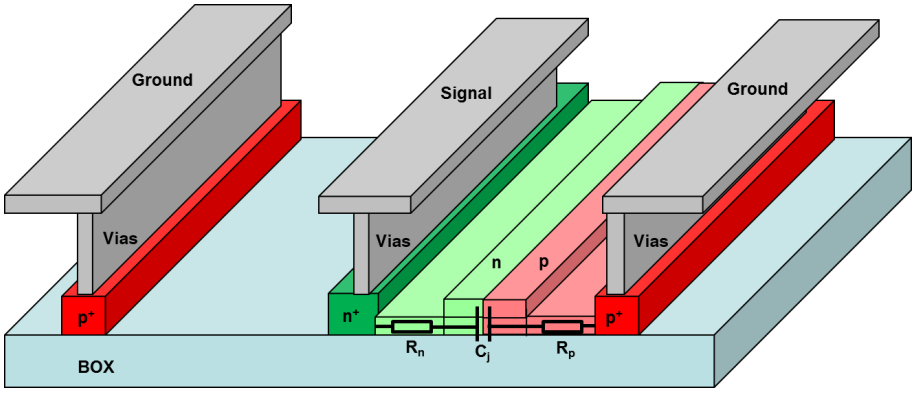

Figure 6. 3-D view of the phase shifter. Analysis of the intrinsic RC-limit caused by the electrical properties of the depletion region in the optical waveguide.

5 Analysis of the RC-limit of the modulator

The high-speed performance of the optical modulator depends on factors like: bandwidth and loss of the transmission lines (TLs), similar velocity of the optical and electrical signal for long phase shifters, loss of the optical waveguides, a good matching between the characteristic impedance of the TL and the modulator driver or the termination impedance (in this work we measure the device on wafer with a termination impedance of 50 Ω) and the intrinsic RC-limit caused by electrical properties of the depletion region in the optical waveguide.

The total resistance per unit length R of the slabs of the optical waveguide symmetrically doped are calculated using Eq. (1) for different lengths of the lowly doped region in the slabs with $h_{sl} = 50$ nm. As expected the resistance is reduced for higher doping concentrations and increases with the lowly doped slab length (Fig. 7a). The contribution of the p-doped region in the total resistance is higher than the n-doped due to the resistivity of p-doped is around twice higher than for n-doped for the same doping concentration.

The junction capacitance of the modulator C_j per unit length of the phase shifter is calculated by

$$C_j = \frac{A}{L} \cdot \sqrt{\frac{q\varepsilon_0\varepsilon_{r_{Si}} N_a N_d}{2\,(N_a + N_d)\,(V_{bi} - V)}} \tag{3}$$

where $A = h \cdot L$ is the cross section area of the pn-junction. The thickness of the cross section is $h = 250$ nm since the pn-junction is formed in the waveguide core and the depletion width is smaller than the waveguide core width w. L is the length of the phase shifter, ε_0 and $\varepsilon_{r_{Si}}$ are the permittivity of the free space and the dielectric constant of silicon, q is the elementary charge, V_{bi} is the built-in potential voltage and V is the applied voltage. The junction capacitance is calculated for the pn-junction in the center of the waveguide depending on the applied reverse bias voltage. In Fig. 7b C_j is plotted for the applied voltages (1–6 V) varying the acceptor concentration for fixed donor concentration of $N_d = 1 \times 10^{17}$ cm^{-3} (blue curves) and $N_d = 1 \times 10^{18}$ cm^{-3} (red curves). The intrinsic 3 dB bandwidth (cutoff frequency f_c) is calculated according to

$$f_c = \frac{1}{2\pi R_s C} \tag{4}$$

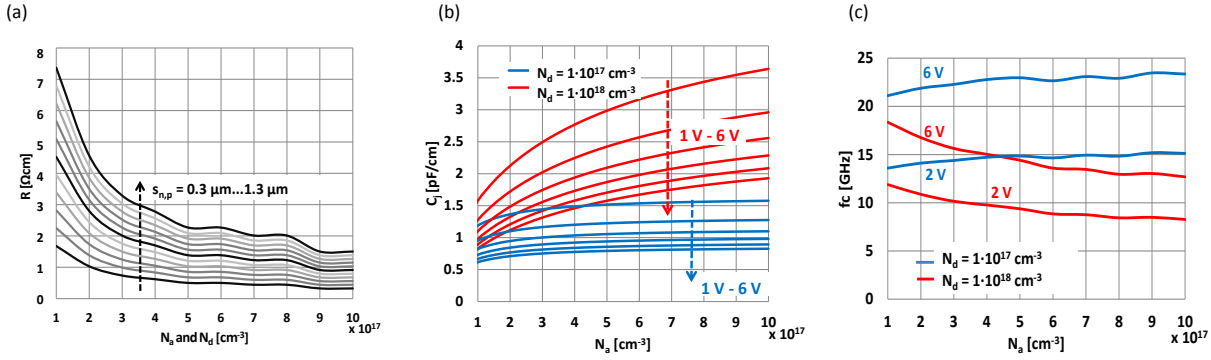

Figure 7. **(a)** Total resistance in Ωcm (normalized with the phase shifter length) of the symmetrically p- and n-doped slabs with $h_{\mathrm{sl}} = 50\,\mathrm{nm}$ for different doping concentrations and slab lengths. **(b)** Junction capacitance per unit length of the phase shifter and **(c)** cutoff frequency depending on the doping concentration and reverse bias voltage for a pn-junction in the center of the waveguide core for a length of the phase shifter of $L = 1\,\mathrm{mm}$ and $s_{\mathrm{n,p}} = 1.25\,\mu\mathrm{m}$.

for the reverse bias voltages 2 and 6 V, being C the junction capacitance in pF ($C = C_j \cdot L$). The donor concentration is the same as in Fig. 7b and the corresponding value of the C_j of this figure is used for the calculation of the cutoff frequency of Fig. 7c. The series resistance R_{s} is calculated using Eq. (1) by

$$R_{\mathrm{s}} = \frac{R}{L} + 50\Omega = \frac{R_{\mathrm{n}} + R_{\mathrm{p}}}{L} + 50\Omega = \frac{\left(\frac{s_{\mathrm{n}} \cdot \rho_{\mathrm{n}}}{h_{\mathrm{sl}}} + \frac{s_{\mathrm{p}} \cdot \rho_{\mathrm{p}}}{h_{\mathrm{sl}}}\right)}{L} + 50\Omega \tag{5}$$

for a phase shifter length of $L = 1\,\mathrm{mm}$ and a slab length of $s = s_{\mathrm{n}} = s_{\mathrm{p}} = 1.25\,\mu\mathrm{m}$. The 50 Ω load impedance is added in the calculation of R_{s}. For a donor concentration of $N_{\mathrm{d}} = 1 \times 10^{17}\,\mathrm{cm}^{-3}$ the cutoff frequency shows only a weak dependence on the acceptor concentration. At 6 and 2 V reverse bias voltages cutoff frequencies of 23 GHz ($C = 0.0826$ pF and $R_{\mathrm{s}} = 82.5$ Ω) and 15 GHz ($C = 0.128$ pF and $R_{\mathrm{s}} = 82.5$ Ω) are achieved for a phase shifter length $L = 1\,\mathrm{mm}$, $s_{\mathrm{n,p}} = 1.25\,\mu\mathrm{m}$, $N_{\mathrm{d}} = 1 \times 10^{17}\,\mathrm{cm}^{-3}$ and $N_{\mathrm{a}} = 10 \times 10^{17}\,\mathrm{cm}^{-3}$. For a higher donor concentration of $N_{\mathrm{d}} = 1 \times 10^{18}\,\mathrm{cm}^{-3}$ the increase of the junction capacitance due to the higher doping does not compensate the decrease in the resistance and therefore lower values of f_{c} are achieved.

The analytical calculation of the junction capacitance for the waveguide with p-doped core (Fig. 5a left) is more complicated because of the different heights of the p- and n-doped regions. To simplify the calculation a conversion of the pn-junction is realized, where the height of the p-side is adapted as shown Fig. 8a and the doping of the p-side is transformed by

$$N'_{\mathrm{a}} = N_{\mathrm{a}} \frac{h}{h_{\mathrm{sl}}}. \tag{6}$$

The relative width of the depletion region depending on the newly adapted doping is calculated as

$$d_{\mathrm{n}} = w_{\mathrm{dep}} \frac{N'_{\mathrm{a}}}{N_{\mathrm{d}} + N'_{\mathrm{a}}} \quad \text{and} \quad d_{\mathrm{p}} = w_{\mathrm{dep}} \frac{N_{\mathrm{d}}}{N_{\mathrm{d}} + N'_{\mathrm{a}}}. \tag{7}$$

The depletion width w_{dep} is

$$w_{\mathrm{dep}} = \sqrt{\frac{2q\varepsilon_0\varepsilon_r(N_{\mathrm{a}+}N_{\mathrm{d}})(V_{\mathrm{bi}} - V)}{qN_{\mathrm{a}}N_{\mathrm{d}}}}. \tag{8}$$

Then, the total junction capacitance is divided into three new capacitances as shown Fig. 8b and calculated by

$$C_j = \frac{1}{\frac{1}{C_{j1}} + \frac{1}{C_{j2}}} + C_{j3}. \tag{9}$$

The numeric expressions for the relative capacitances C_{j1}, C_{j2} and C_{j3} are calculated using the method of conformal mapping as described by (Yu and Bogaerts, 2012) including the effect of the electrical field out of the pn-junction (C_{ch}) described in Chang (1976)

$$C_{j1} = \left(C_{\mathrm{Ch1}} - \varepsilon_0\varepsilon_{r,\mathrm{Si}}\frac{h}{d_{\mathrm{p}}}\right)\frac{\varepsilon_{r,\mathrm{SiO_2}}}{\varepsilon_{r,\mathrm{Si}}} + \varepsilon_0\varepsilon_{r,\mathrm{Si}}\frac{h}{d_{\mathrm{p}}},\ C_{j2} = \left(C_{\mathrm{Ch2}} - \varepsilon_0\varepsilon_{r,\mathrm{Si}}\frac{h}{d_{\mathrm{n}}}\right)\frac{\varepsilon_{r,\mathrm{SiO_2}}}{\varepsilon_{r,\mathrm{Si}}} + \varepsilon_0\varepsilon_{r,\mathrm{Si}}\frac{h}{d_{\mathrm{n}}} \tag{10}$$

and

$$C_{j3} = \frac{1}{2}\left(C_{\mathrm{Ch3}} - \varepsilon_0\varepsilon_{r,\mathrm{SiO_2}}\frac{h_{\mathrm{sl}}}{w_{\mathrm{dep}}/2}\right). \tag{11}$$

At 0 V bias voltage the total junction capacitance of the fabricated device described in the next section (Fig. 10) is

$$C_j = \frac{1}{\frac{1}{9.19\,\frac{\mathrm{pF}}{\mathrm{cm}}} + \frac{1}{1.078\,\frac{\mathrm{pF}}{\mathrm{cm}}}} + 0.076\frac{\mathrm{pF}}{\mathrm{cm}} \approx 1.04\frac{\mathrm{pF}}{\mathrm{cm}}. \tag{12}$$

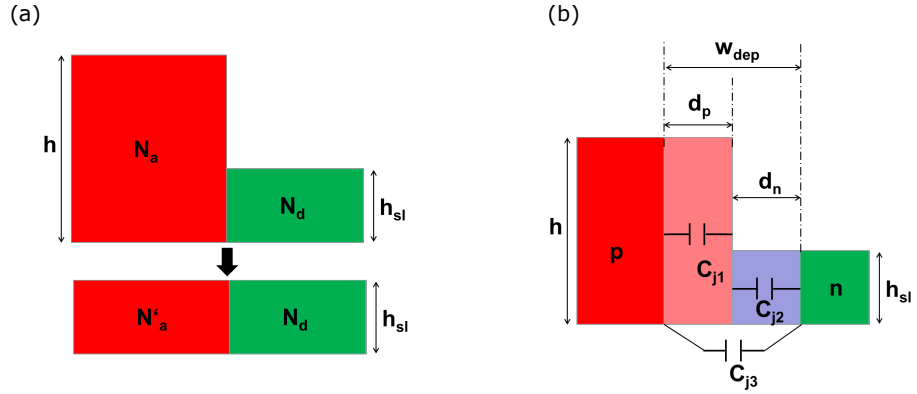

Figure 8. (a) Modification of the lateral pn-junction. **(b)** Relative capacitances for the simplification of the calculation of the total junction capacitance.

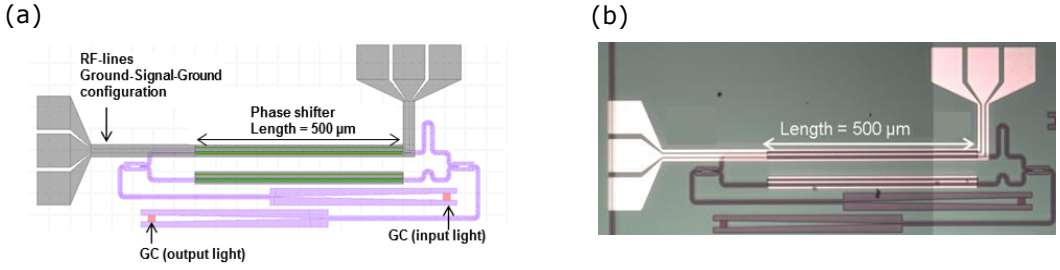

Figure 9. (a) Layout of a MZM with a phase shifter length of 500 µm, **(b)** MZM micrograph.

The same cross section is simulated using the software CST-Microwave Studio with a result of 1.01 $\frac{\text{pF}}{\text{cm}}$ for an ideal pn-junction of the structure. This matches well with the analytical model. The series resistance is $R_s = 79\ \Omega$ ($s_{n,p} = 400\,\text{nm}$; $h_{sl} = 80\,\text{nm}$). Therefore, the expected cutoff frequency at 0 V bias voltage is 39 GHz. For higher bias voltages the junction capacitance is reduced ($C_j\ (2\,\text{V}) = 0.65\,\frac{\text{pF}}{\text{cm}}$ and $C_j\ (6\,\text{V}) = 0.49\,\frac{\text{pF}}{\text{cm}}$) and the calculated cutoff frequencies are $f_c\ (2\,\text{V}) = 62\,\text{GHz}$ and $f_c\ (6\,\text{V}) = 82\,\text{GHz}$.

6 Fabricated structure and measurement results

First designed optical modulator in IMS CHIPS technology is successfully measured. The device is fabricated as a prototype to prove the accuracy of the simulations and the functionality of the used technology. The layout and micrograph of the complete MZM with a 500 µm long phase shifter is shown in Fig. 9. The cross-section of the phase modulator is presented in Fig. 10.

The target doping concentrations in the p- and n-doped regions are $1 \times 10^{17}\,\text{cm}^{-3}$. In this design the distances $s = 0.7\,\mu\text{m}$ and $s_{p,n} = 0.4\,\mu\text{m}$ are smaller the optimum dimensions shown in the previous simulations (Fig. 4). Besides, instead of the target slab thickness $h_{sl} = 50\,\text{nm}$, the fabricated structure has a slab thickness of 80 nm due to fabrication deviations during the silicon etching process. Therefore, higher optical loss is expected for this device (see Fig. 2b and Fig. 4b).

For DC measurements a DC voltage source is connected through a bias-T to a ground-signal-ground (GSG) probe. The optical transmission spectrum for different reverse bias voltages is plotted in Fig. 11. The fiber-to-fiber insertion loss (IL) of the entire MZM, that includes the losses of the gratings, tapers and MMIs, is 12.5 dB for $\lambda = 1550\,\text{nm}$. The GC used for this design is a standard one, therefore the total loss could be reduced by using the high efficient couplers ($\eta = -0.74\,\text{dB}$ at $\lambda = 1550\,\text{nm}$) developed by our group in the same technology (Zaoui et al., 2014) reducing the total loss of the modulator by approximately 6 dB. The IL on-chip is 4.2 dB for 0 V bias. The loss of the phase shifter is about $2\,\text{dB mm}^{-1}$. The passive ER is around 32 dB and the modulation efficiency is $V_\pi L = 3.1\,\text{V·cm}$ at 2 V reverse bias voltage. The simulated modulation efficiency for this structure is $V_\pi L = 2.87\,\text{V·cm}$ with a loss of $1\,\text{dB mm}^{-1}$. The difference with the measured one is probably caused by irregularities in the doping or misalignment of the doping masks during fabrication. Same simulations are realized with a horizontal shift of $\sim 150\,\text{nm}$ of the highly doping mask and similar results as the measured ones are demonstrated.

The frequency response of the MZM is examined. High frequency measurements of the coplanar waveguides (CPW)

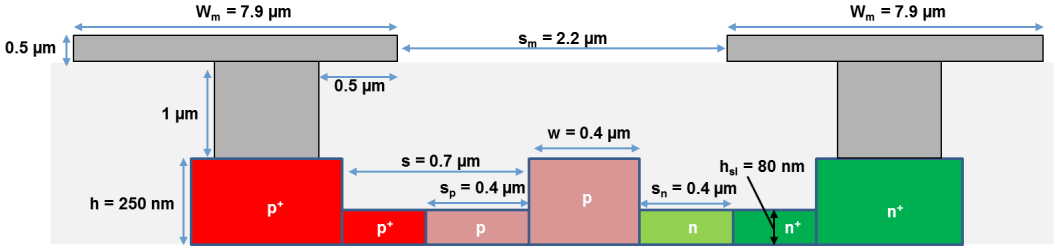

Figure 10. Cross section of the fabricated phase modulator.

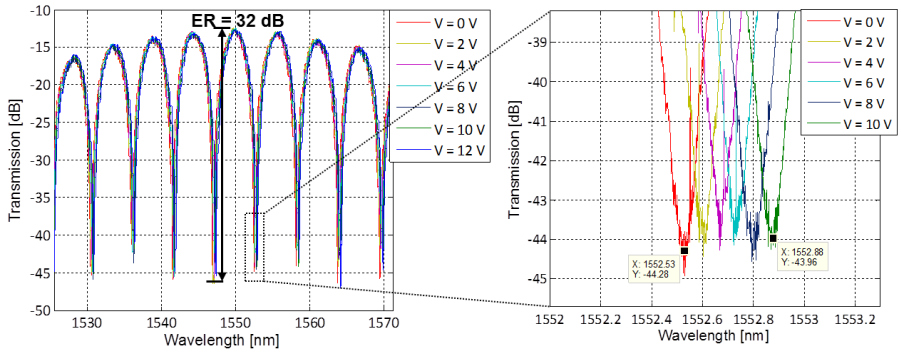

Figure 11. Measurement of the optical transmission of the MZM for different reverse bias voltages.

working as traveling wave electrodes (TWEs) of the modulator are realized for different bias voltages. The measurements of the TWEs are compared in Fig. 12 with the response of the TL with the same dimensions ($W_m = 7.9\,\mu m$ and $s_m = 2.2\,\mu m$) without the MZM under the RF coplanar lines. The TL shows a similar transmission than the TWEs of the optical modulator. The difference is the resonance of the TWEs around 30 GHz. The doped silicon ridge waveguide used to modulate the light using the plasma dispersion effect works as a diode. In the core of the waveguide there is a depletion region caused by the reverse bias voltage applied to the waveguide through the TWEs. By increasing the supply voltage, the depletion region becomes wider. Consequently, the variable junction capacitance decreases and the electrical transmission of the modulator improves. In addition, the asymmetric configuration of the modulator favors the mode conversion of the CPW mode (in Fig. 13a position 1 with symmetric CPW) to the unwanted coupled-slotline (CSL) mode (in Fig. 13a position 2 with asymmetry because of the diode under the CPW). That also explains that in the case of the TL without modulator under the lines, therefore symmetric, the resonance is not observed. To suppress this CSL mode, air-bridges could be used to flatten the frequency response curve and thus increase the bandwidth (Jongjoo Lee et al., 1999; Hao Xu et al., 2014). Therefore, the bandwidth of the device calculated in Sect. 5 could be achieved if this undesired effect is diminished. This is difficult because the ground lines have a width smaller than 8 µm. That is too small for the use of bond wires to minimize this effect. Nevertheless, in future designs this fact should be taken into account to avoid undesirable effects using symmetric CPW as presented in Fig. 13b.

If the velocities of the driving electrical signal and optical wave match perfectly, the 6.4 dB-electrical bandwidth of the TWEs corresponds to the 3 dB-electro-optical bandwidth of the modulator. The 6.4 dB-electrical bandwidth of the modulator for the voltage range from 0 to 2 V is 30 GHz. However, for higher voltages like 8 V (green curve) a bandwidth higher than 50 GHz can be reached. The reflection of the TWEs keeps below −10 dB up to 50 GHz.

New dimensions of the transmission lines are simulated to improve the performance with respect to the bandwidth and loss by using the software Momentum of Advance Design System (ADS). The dimensions are based on the previous simulations of the optical doped waveguide, since the distance between the metal lines depends on the length of the slabs ($s = 1.25\,\mu m$). Therefore, the space between the metal lines s_m is kept lower than 2.9 µm. The optimized coplanar line is fabricated and measured on wafer using RF-probes with a pitch of 100 µm. The new transmission line is also designed as an L-shape line (Fig. 9 and Fig. 14), based on the measurement setup used. In Fig. 15 the measurement results are compared with the dimensions of the coplanar TL presented before (Fig. 12). With a line width of $W_m = 16.7\,\mu m$ and a distance between the metal lines of $s_m = 2.8\,\mu m$ the loss of the line is at 50 GHz less than 3.2 dB and approx-

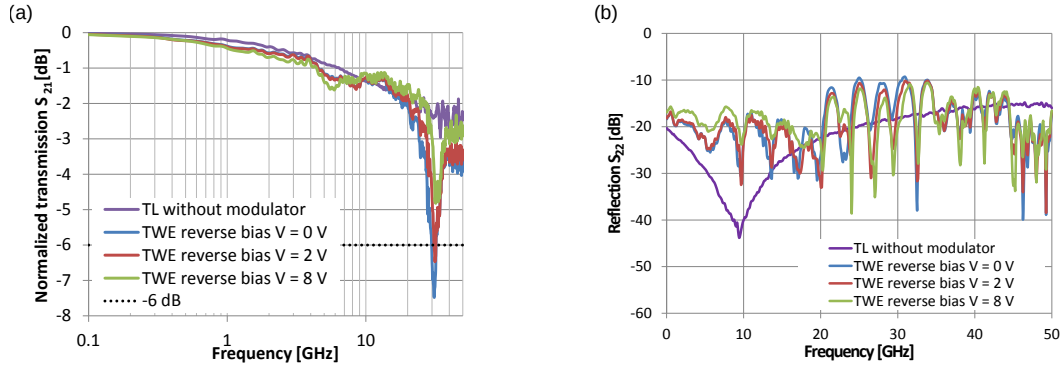

Figure 12. Measurement of the transmission **(a)** and reflection **(b)** of the TL and the TWEs of the modulator with same dimensions for different applied voltages.

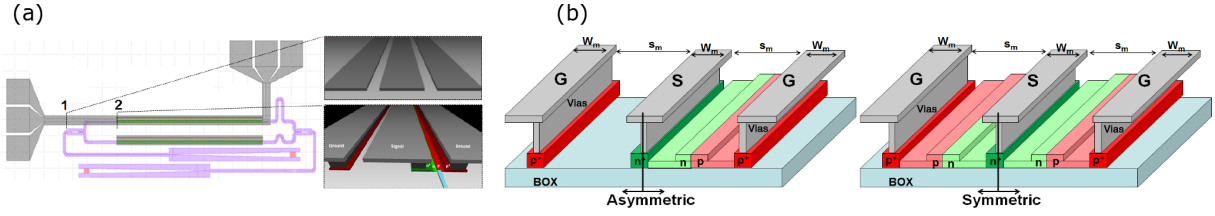

Figure 13. (a) Layout MZM. Position 1: Symmetric CPW. Position 2: Start of the phase shifter, the CPW is not symmetric along the phase shifter because of the diode (pn-junction) under the metal lines. **(b)** Asymmetric and symmetric CPW.

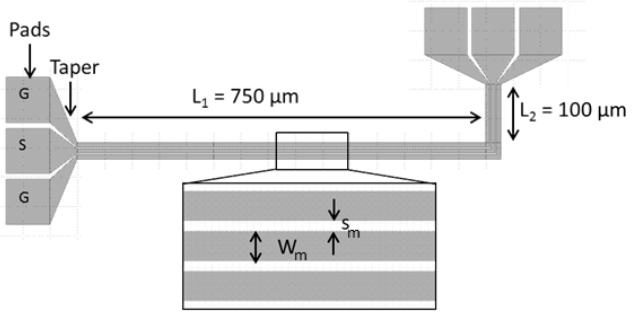

Figure 14. Scheme of the measured aluminum coplanar waveguide.

imately 0.5 dB at low frequencies. Both lines have a 3 dB bandwidth greater than 50 GHz. The new design offers a better frequency response with a lower loss in the whole measured spectrum and the reflection is kept lower than −20 dB up to 50 GHz.

7 Optimization using different doping concentrations for p- and n-doped regions – influence in the modulation performance and optical loss of the distance from waveguide core to the highly doped regions

For the optimization of the structure new simulations are realized varying the doping concentration and the distance s_n and s_p to the highly doped regions. In the new design this distance is reduced to $s_n = s_p = 0.5\,\mu m$ and the distance to metal contacts is $s = 1.25\,\mu m$ (Fig. 16). So, the highly doped regions are present in the slabs. The Δn_{eff} and the optical loss α of the structure are simulated depending on the acceptor concentration N_a of the p-doped region for two different donor concentrations ($N_d = 1 \times 10^{17}\,cm^{-3}$ and $N_d = 1 \times 10^{18}\,cm^{-3}$) of the n-doped region. The highly doped regions have concentrations of $N_{a+,d+} = 1 \times 10^{20}\,cm^{-3}$. The simulation results are plotted in Fig. 17. The change of the effective index is similar for a low acceptor doping concentration ($N_a = 5 \times 10^{16}\,cm^{-3}$). However, for the case of $N_d = 1 \times 10^{18}\,cm^{-3}$ the Δn_{eff} increase till around twice the value for the $N_d = 1 \times 10^{17}\,cm^{-3}$ curve achieving a Δn_{eff} of around 2.5×10^{-4} (Fig. 17a). The loss regarding the free carrier absorption increases with the doping concentration as expected. The offset between both curves is kept constant for the simulated range of N_a (Fig. 17b). As comparison, the modulation efficiency and the figure of merit $V_\pi L \cdot \alpha$ are plotted in Fig. 17c. Looking at this plot an optimal doping concentration can be chosen taking into account the modulation efficiency and loss. For example, a promising configuration is $N_d = 1 \times 10^{18}\,cm^{-3}$ and $N_a = 9 \times 10^{16}\,cm^{-3}$ since a low $V_\pi L$ of around 1.8 V·cm at 6 V is achieved with a $V_\pi L \cdot \alpha \approx 6\,V{\cdot}dB$.

Finally, the distance from the waveguide core to the highly doped regions s_p and s_n is examined. Simulations to determine the optimum value for these parameters are re-

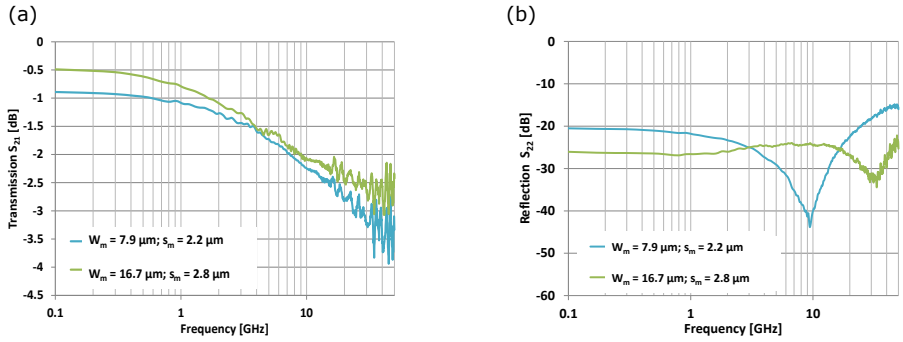

Figure 15. Measurement results of the **(a)** transmission and **(b)** reflection vs. frequency for the structure in Fig. 14.

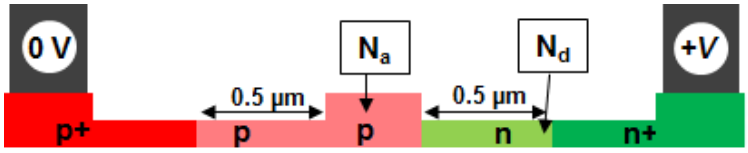

Figure 16. Scheme of the simulated structure. $s_{\mathrm{p}} = s_{\mathrm{n}} = 0.5\,\mu\mathrm{m}$, $s = 1.25\,\mu\mathrm{m}$, $h_{\mathrm{sl}} = 50\,\mathrm{nm}$, $N_{\mathrm{a+,d+}} = 1 \times 10^{20}\,\mathrm{cm}^{-3}$.

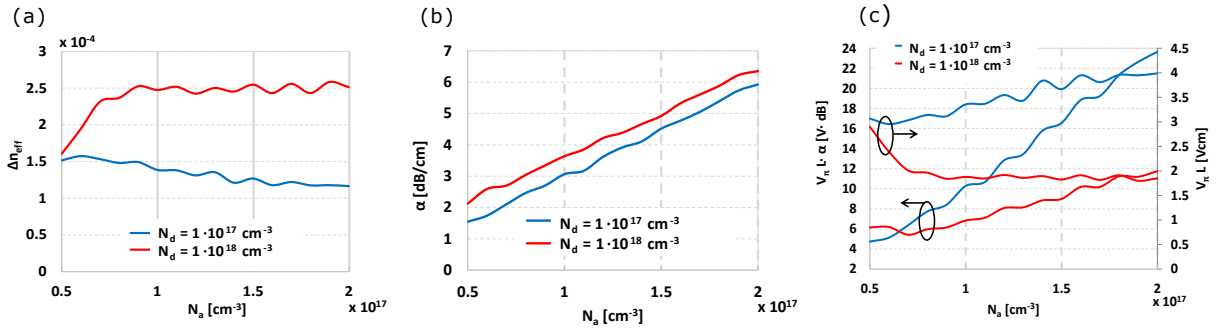

Figure 17. Simulations of **(a)** the change of the effective refractive index at 6 V, **(b)** the attenuation at 0 V, **(c)** modulation efficiency and $V_\pi L \cdot \alpha$ of the structure shown in Fig. 16 varying the acceptor doping density N_{a} for two donor doping densities N_{d}.

alized for the optimized doping $N_{\mathrm{a}} = 9 \times 10^{16}\,\mathrm{cm}^{-3}$ and $N_{\mathrm{d}} = 1 \times 10^{18}\,\mathrm{cm}^{-3}$. The scheme of the simulated structure is presented in Fig. 18. With these simulations (Fig. 19) it is proven that the distance $s_{\mathrm{p,n}} = 0.5\,\mu\mathrm{m}$ taken in Fig. 16 is a good value. But still a small improvement could be achieved by increasing this distance to $s_{\mathrm{p,n}} = 0.6\,\mu\mathrm{m}$. The loss is $\alpha = 0.31\,\mathrm{dB\,mm}^{-1}$. This small difference in the $s_{\mathrm{p,n}}$ distance has not a notable influence in the modulation efficiency ($V_\pi L = 1.8\,\mathrm{V{\cdot}cm}$) and a value of $V_\pi L \cdot \alpha \approx 5.8\,\mathrm{V{\cdot}dB}$ is obtained. However, the bandwidth is slightly reduced for short modulators due to the increase of the series resistance of the device. For $s_{\mathrm{p,n}} = 0.5\,\mu\mathrm{m}$, the calculated bandwidth for a phase shifter length of 0.5 mm is $f_{\mathrm{c}}\,(2\,\mathrm{V}) = 27\,\mathrm{GHz}$ and $f_{\mathrm{c}}\,(6\,\mathrm{V}) = 39\,\mathrm{GHz}$. For the case of $s_{\mathrm{p,n}} = 0.6\,\mu\mathrm{m}$ the bandwidth is 25 and 36 GHz at 2 and 6 V, respectively. For modulators with long phase shifters (~ 3 mm) the difference in the bandwidth due to this fact is negligible.

Thus, the final structure has a waveguide core width of $w = 400\,\mathrm{nm}$ and is p-doped. The slabs have a width of $s = 1.25\,\mu\mathrm{m}$ and a thickness of $h_{\mathrm{sl}} = 50\,\mathrm{nm}$. The highly doped regions are separated from the waveguide core at a distance of $s_{\mathrm{p,n}} = 0.6\,\mu\mathrm{m}$. The doping concentrations are $N_{\mathrm{a+,d+}} = 10^{20}\,\mathrm{cm}^{-3}$, $N_{\mathrm{a}} = 9 \times 10^{16}\,\mathrm{cm}^{-3}$ and $N_{\mathrm{d}} = 1 \times 10^{18}\,\mathrm{cm}^{-3}$. For a 6 V reverse bias voltage the change of the effective refractive index is $\Delta n_{\mathrm{eff}} = 2.5 \times 10^{-4}$. Therefore, a phase shift $\Delta\varphi = \pi$ is obtained for a phase shifter length of

$$L_\pi = \frac{\lambda}{2\Delta n_{\mathrm{eff}}} \approx 3.1\,\mathrm{mm} \tag{13}$$

Thus, the modulation efficiency of the modulator is $V_\pi L = 1.8\,\mathrm{V{\cdot}cm}$. The calculated cutoff frequency of the modulator with a phase shifter length of 3.1 mm is 7 and 10 GHz at 2 and 6 V. The calculated optical loss of the phase shifter for the length L_π is 0.97 dB at 0 V. The fiber-to-fiber

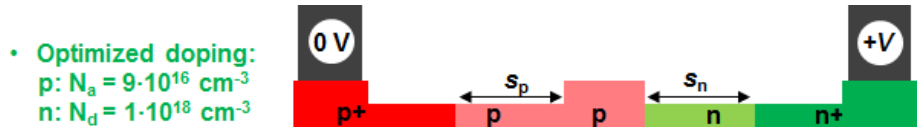

Figure 18. Scheme of the simulated structure. The distance $s_{p,n}$ is varied. $N_a = 9 \times 10^{16}\,\mathrm{cm}^{-3}$, $N_d = 1 \times 10^{18}\,\mathrm{cm}^{-3}$, $N_{a+,d+} = 1 \times 10^{20}\,\mathrm{cm}^{-3}$, $s = 1.25\,\mu\mathrm{m}$, $h_{sl} = 50\,\mathrm{nm}$.

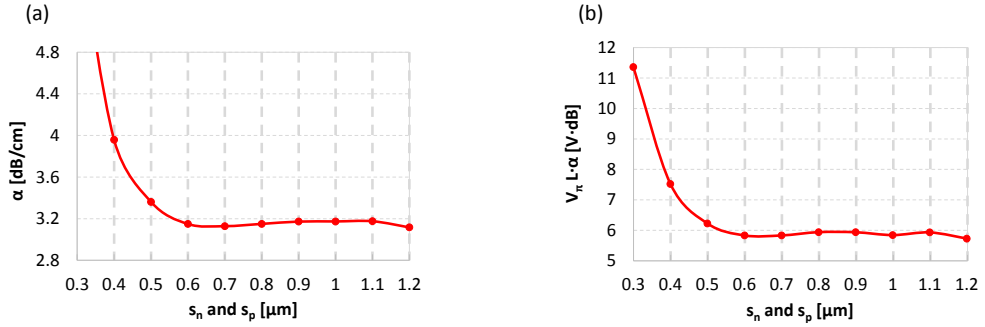

Figure 19. Simulation of **(a)** the optical loss regarding the free carrier absorption at 0 V and **(b)** $V_\pi L \cdot \alpha$ vs. the distance from the core to the area with high doping concentration for the structure in Fig. 18.

loss of the modulator is determined as the sum of the calculated phase shifter loss and the losses of the previously designed and measured optical components (i.e., grating couplers, MMIs, waveguides and tapers) in the used technology. The measured loss at $\lambda = 1.55\,\mu\mathrm{m}$ of the grating couplers is 0.74 dB/coupler and 0.05 dB/MMI. The coupling loss between the 400 nm width strip waveguide and the ridge waveguide of the phase shifter is 0.05 dB/coupling. The linear taper with a length of 400 µm has a loss of 0.4 dB and the waveguide loss due to the roughness and other imperfections during the fabrication process is $3.3\,\mathrm{dB\,cm}^{-1}$. Considering a phase shifter length of 3.1 and 1 mm of additional undoped waveguides an ultra-low fiber-to-fiber loss of approximately 4.8 dB is expected for the complete modulator fabricated in this technology.

8 Comparison with other technologies

Silicon optical modulators based on the carrier-depletion effect have been developed by different research groups in the last years. High-speed modulations up to $60\,\mathrm{Gbit\,s}^{-1}$ have been demonstrated (Xiao et al., 2013) by properly choosing the doping concentration and precisely locating the junction. Modulators based on the slow light effect can be integrated on a very small area and exhibit a very low $V_\pi L$ of 0.85 V·cm (Brimont et al., 2012; Akiyama et al., 2012). However, the loss is higher than for other modulators of the same length. Some of the device developed during the last years are presented as a comparison in Table 1 based on the publication (Azadeh et al., 2015a). Different doping profiles and concentrations are used. The pn-diode in the optical waveguide can be designed in vertical direction (Liao et al., 2007; Azadeh et al., 2015b), lateral direction (Samani et al., 2015; Tu et al., 2014; Wang et al., 2013) or with interdigitated doping patterns (Xu et al., 2012; Hao Xu et al., 2014; Giesecke et al., 2016). Some important figures of merit of the modulator and geometry dimensions of the published devices are presented in Table 1 and compared with the results of this work.

9 Conclusions

The design and simulations of a single-drive carrier-depletion MZM in a 250 nm SOI technology with a modulated phase shifter in one branch of the device is presented. The influences of the ridge waveguide dimensions and the doping of the device are studied. An analysis of the RC-limit of the modulator for different doping profiles is described. A MZM is fabricated and measured showing a modulation efficiency of 3.1 V·cm with an optical loss of $\alpha = 2\,\mathrm{dB\,mm}^{-1}$. The length of the phase shifter is 0.5 mm. The on-chip insertion loss of the modulator is 4.2 dB. The electrical bandwidth of the modulator is 30 GHz. RF coplanar lines with a 3 dB bandwidth higher than 50 GHz are designed and measured. Finally, simulations to optimize the modulation efficiency and optical loss are realized achieving a theoretical modulation efficiency of $V_\pi L = 1.8$ V·cm and a maximum optical loss due to the free carriers of $\alpha = 0.31\,\mathrm{dB\,mm}^{-1}$. The expected fiber-to-fiber loss of a MZM with a phase shifter length of 3.1 mm is approximately 4.8 dB.

Table 1. State of the art of carrier-depletion phase shifter designs on different SOI technologies for $\lambda = 1550$ nm.

Type	h [nm]	L [mm]	h_{sl} [nm]	$s_{n,p}$ [µm]	α [dB mm^{-1}]	Optical loss [dB]	$V_\pi L$ [V·cm]	f_c [GHz] (bias V)	Reference
Lateral	220	2.5 1.25	90	0.8	2	6.5[5]/15.5[7] 4.5[5]/13.5[7]	2 (2 V) 2.25 (2 V)	17 (2 V) 23 (2 V)	Azadeh et al. (2014)
Lateral	220	1	100	–	2.8	3.9[6]	1.72 (2 V)	30 (2 V)	Wang et al. (2013)
Lateral	220	5.5	100	–	0.94	5.2[6]	2.2 (4 V)	24 (5 V)	Tu et al. (2014)
Lateral	220	0.5	100	$s_p = 0.5$ $s_n = 0.55$	10	6[5]	0.85 (5 V)	Data rate: 40 Gbit s^{-1}	Brimont et al. (2012)
Lateral	220	4.2	90	0.95	1.1	4.5[6]/14.7[7]	3.15 (7.5 V)	35 (3 V)	Samani et al. (2015)
Lateral[2]	220	2.4	100	–	7.1	17[6]	0.97 (0–2 V)	61 (1 V)[4]	Azadeh et al. (2015a)
Interd.[1]	340	0.75	80	1	1	2[6]	1.62 (2 V)	20 (3 V)	Xu et al. (2012)
Interd.[1]	220	1	90	0.6	2.8	3.8[5]	2.2 (2 V)	30 (3 V)	Hao Xu et al. (2014)
Interd.[1]	220	2	45	–	1.1 0.65	2.2[6] 1.3[6]	0.6 (2 V) 0.74 (2 V)	5 (2 V) 3 (2 V)	Giesecke et al. (2016)
Vertical	290	1.8	–	0.8	4.2	6.7[6]	0.74 (0–2 V)	48 (1 V)[4]	Azadeh et al. (2015a)
Vertical	500	1	–	1	1.8	<4[5]/10[7]	<4	30 (3 V)	Liao et al. (2007)
Lateral	250	0.5	80	0.4	2	4.2[5]/12.5[7]	3.1 (2 V)	30 (2 V); >50 (6 V)	This work
Lateral[2]	250	3.1	50	0.6	0.31[3]	4.8[7]	1.8 (6 V)	10 (6 V)[4]	This work
Lateral[2]	250	0.5	50	0.6	0.31[3]	3.1[7]	1.8 (6 V)	36 (6 V)[4]	This work

[1] Interdigitated. [2] Simulated/calculated. [3] Only free carrier absorption at 0 V. [4] Intrinsic cutoff frequency. [5] On-chip loss. [6] Insertion loss. [7] Fiber-to-fiber loss.

Data availability. The measurement data and simulation data that support the findings of this study are available in Zenodo with the identifier https://doi.org/10.5281/zenodo.1037908 (Félix Rosa et al., 2017).

Competing interests. The authors declare that they have no conflict of interest.

Edited by: Dirk Killat
Reviewed by: three anonymous referees

References

Akiyama, S., Baba, T., Imai, M., Akagawa, T., Noguchi, M., Saito, E., Noguchi, Y., Hirayama, N., Horikawa, T., and Usuki, T.: 50-Gb/s silicon modulator using 250-µm-Long phase shifter based-on forward-biased pin diodes, in: 2012 IEEE 9th International Conference on Group IV Photonics (GFP), San Diego, CA, USA, 192–194, 2012.

Azadeh, S. S., Müller, J., Merget, F., Romero-García, S., Shen, B., and Witzens, J.: Advances in silicon photonics segmented electrode Mach-Zehnder modulators and peaking enhanced resonant devices, in: Photonics North 2014, edited by: MacLean, S. and Plant, D. V., Montréal, Canada, Wednesday 28 May 2014, SPIE Proceedings, SPIE, 928817, 2014.

Azadeh, S. S., Merget, F., Romero-Garcia, S., Moscoso-Martir, A., den Driesch, N. von, Muller, J., Mantl, S., Buca, D., and Witzens, J.: Low V(pi) Silicon photonics modulators with highly linear epitaxially grown phase shifters, Opt. Express, 23, 23526–23550, https://doi.org/10.1364/OE.23.023526, 2015a.

Azadeh, S. S., Romero-García, S., Merget, F., Moscoso-Mártir, A., den Driesch, N. von, Buca, D., and Witzens, J.: Epitaxially grown vertical junction phase shifters for improved modulation efficiency in silicon depletion-type modulators, in: SPIE Optics + Optoelectronics, edited by: Cheben, P., Čtyroký, J., and Molina-Fernández, I., Prague, Czech Republic, Monday 13 April 2015, SPIE Proceedings, SPIE, 95160T, 2015b.

Brimont, A., Thomson, D. J., Gardes, F. Y., Fedeli, J. M., Reed, G. T., Marti, J., and Sanchis, P.: High-contrast 40 Gb/s operation of a 500 mum long silicon carrier-depletion slow wave modulator, Opt. Lett., 37, 3504–3506, https://doi.org/10.1364/OL.37.003504, 2012.

Chang, W. H.: Analytical IC Metal-Line Capacitance Formulas (Short Papers), IEEE Trans. Microwave Theory Techn., 24, 608–611, https://doi.org/10.1109/TMTT.1976.1128917, 1976.

Félix Rosa, M., Rathgeber, L., Elster, R., Hoppe, N., Föhn, T., Schmidt, M., and Berroth, M.: Data set of a carrier-depletion Mach-Zehnder modulator in 250 nm silicon-on-insulator technology, available at: https://doi.org/10.5281/zenodo.1037908, 2017.

Giesecke, A. L., Prinzen, A., Füser, H., Porschatis, C., Lerch, H., Bolten, J., Suckow, S., Chmielak, B., and Wahlbrink, T.: Ultra-efficient Interleaved Depletion Modulators by Using Advanced Fabrication Technology: 42nd European Conference on Optical Communication September 18–22, 2016, Congress Center Düsseldorf (CCD), Germany; proceedings, VDE Verlag, Berlin, Offenbach, 1 pp., 2016.

Goykhman, I., Desiatov, B., Ben-Ezra, S., Shappir, J., and Levy, U.: Optimization of efficiency-loss figure of merit in carrier-depletion silicon Mach-Zehnder optical modulator, Opt. Express, 21, 19518–19529, https://doi.org/10.1364/OE.21.019518, 2013.

Lee, J., Lee, H., Kim, W., Lee, J., and Kim, J.: Suppression of coupled-slotline mode on CPW using air-bridges measured by picosecond photoconductive sampling, IEEE Microw. Guid. Wave Lett., 9, 265–267, https://doi.org/10.1109/75.774141, 1999.

Liao, L., Liu, A., Rubin, D., Basak, J., Chetrit, Y., Nguyen, H., Cohen, R., Izhaky, N., and Paniccia, M.: 40 Gbit s^{-1} silicon optical modulator for high-speed applications, Electron. Lett., 43, 1196, https://doi.org/10.1049/el:20072253, 2007.

Petousi, D., Zimmermann, L., Voigt, K., and Petermann, K.: Performance Limits of Depletion-Type Silicon Mach–Zehnder Modulators for Telecom Applications, J. Lightwave Technol., 31, 3556–3562, https://doi.org/10.1109/JLT.2013.2284969, 2013.

Samani, A., Chagnon, M., Patel, D., Veerasubramanian, V., Ghosh, S., Osman, M., Zhong, Q., and Plant, D. V.: A Low-Voltage 35-GHz Silicon Photonic Modulator-Enabled 112-Gb/s Transmission System, IEEE Photonics J., 7, 1–13, https://doi.org/10.1109/JPHOT.2015.2426875, 2015.

Soref, R. and Bennett, B.: Electrooptical effects in silicon, IEEE J. Quantum Electron., 23, 123–129, https://doi.org/10.1109/JQE.1987.1073206, 1987.

Tu, X., Chang, K.-F., Liow, T.-Y., Song, J., Luo, X., Jia, L., Fang, Q., Yu, M., Lo, G.-Q., Dong, P., and Chen, Y.-K.: Silicon optical modulator with shield coplanar waveguide electrodes, Opt. Express, 22, 23724–23731, https://doi.org/10.1364/OE.22.023724, 2014.

Wang, J., Qiu, C., Li, H., Ling, W., Le Li, Pang, A., Sheng, Z., Wu, A., Wang, X., Zou, S., and Gan, F.: Optimization and Demonstration of a Large-bandwidth Carrier-depletion Silicon Optical Modulator, J. Lightwave Technol., 31, 4119–4125, https://doi.org/10.1109/JLT.2013.2287671, 2013.

Xiao, X., Xu, H., Li, X., Li, Z., Chu, T., Yu, Y., and Yu, J.: High-speed, low-loss silicon Mach-Zehnder modulators with doping optimization, Opt. Express, 21, 4116–4125, https://doi.org/10.1364/OE.21.004116, 2013.

Xu, H., Xiao, X., Li, X., Hu, Y., Li, Z., Chu, T., Yu, Y., and Yu, J.: High speed silicon Mach-Zehnder modulator based on interleaved PN junctions, Opt. Express, 20, 15093–15099, https://doi.org/10.1364/OE.20.015093, 2012.

Xu, H., Li, X., Xiao, X., Li, Z., Yu, Y., and Yu, J.: Demonstration and Characterization of High-Speed Silicon Depletion-Mode Mach–Zehnder Modulators, IEEE J. Select. Topics Quantum Electron., 20, 23–32, https://doi.org/10.1109/JSTQE.2013.2293763, 2014.

Yu, H., Pantouvaki, M., van Campenhout, J., Korn, D., Komorowska, K., Dumon, P., Li, Y., Verheyen, P., Absil, P., Alloatti, L., Hillerkuss, D., Leuthold, J., Baets, R., and Bogaerts, W.: Performance tradeoff between lateral and interdigitated doping patterns for high speed carrier-depletion based silicon modulators, Opt. Express, 20, 12926–12938, https://doi.org/10.1364/OE.20.012926, 2012.

Zaoui, W. S., Kunze, A., Vogel, W., and Berroth, M.: CMOS-Compatible Polarization Splitting Grating Couplers With a Backside Metal Mirror, IEEE Photon. Technol. Lett., 25, 1395–1397, https://doi.org/10.1109/LPT.2013.2266132, 2013.

Zaoui, W. S., Kunze, A., Vogel, W., Berroth, M., Butschke, J., Letzkus, F., and Burghartz, J.: Bridging the gap between optical fibers and silicon photonic integrated circuits, Opt. Express, 22, 1277–1286, https://doi.org/10.1364/OE.22.001277, 2014.